

Multi-Equal-Collision-Probability-Curve[‡] Method for Convex Polygon-shape Spacecraft Safe Proximity Manoeuvres

Wang Yi¹, Chen Xiaoqian¹, Ran Dechao¹, Ou Yangwei¹, Ni Qing² and Bai Yuzhu¹

¹(College of Aerospace Science and Engineering, National University of Defense Technology, Changsha 410073, People's Republic of China)

²(Manned Space System Research Center, Beijing 10000, People's Republic of China)
(E-mail: baiyuzhu@hotmail.com)

In this paper, the spacecraft close-range safe proximity problem is investigated. In the presence of a “chief” spacecraft, a Multi-Equal-Collision-Probability-Curve (MECPC) method is developed. The influence of the chief spacecraft with a convex polygon shape is considered and the chief spacecraft is divided into several small components. Each component generates a corresponding separate repulsive force and the superposition of these forces is regarded as the ultimate avoidance force. As a result, the proposed MECPC method not only improves the system robustness against control and navigation uncertainties but is also analytically validated in collision avoidance. The MECPC method solves the safe proximity problem in the presence of a convex polygon shape. In addition, an Improved Linear Quadratic Regulator (ILQR) is designed to track the expected trajectory. Numerical simulations are performed in a close-range operation environment to verify the effectiveness of the proposed MECPC method.

KEY WORDS

1. Collision Avoidance. 2. Convex Shapes. 3. Close-range Proximity. 4. Collision Probability Density. 5. Equal Collision Probability Curve.

Submitted: 19 February 2018. Accepted: 21 August 2018. First published online: 27 September 2018.

1. INTRODUCTION. Close-range proximity spacecraft flight is a promising technology for on-orbit servicing missions such as space assembly, maintenance, inspection and space debris capture and removal (Flores-Abad et al., 2014; Yu et al., 2015; Shan et al., 2016). To facilitate this, solving the collision avoidance problem is essential. To this end, the Artificial Potential Function (APF) method is popular and has been widely developed (Bevilacqua et al., 2011; Nag and Summerer, 2013; Palacios et al., 2015; Spencer et al.,

[‡] The original version of this article was published with an incorrect title. A notice detailing this has been published and the error rectified in the online and print PDF and HTML copies.

2016; Ni et al, 2016; Huang et al., 2017a; 2017b; Cao et al., 2018). The APF method has several advantages, such as low computing cost and ease of analytical validation. However, the presented potential functions ignore the influence of quantities such as navigation and control uncertainties.

As uncertainties exist in the measurement data (Cao et al., 2018b), the collision probability is always computed to assess the collision risk. According to different scenarios with different relative velocities or different encounter durations, the collision probability computing methods have been divided into short-term encounters (Alfano., 2006a; Bai et al., 2013; 2016; Serra et al., 2016) and long-term encounters (Patera., 2003; 2006; Alfano., 2006b; McKinley, 2006). Researchers have developed many methodologies to decrease the computational burden of collision probability. In terms of non-Gaussian distribution, Demars et al. (2014) and Vittaldev et al. (2016) employed a Gaussian Mixture Model to compute the collision probability. With the collision probability, the optimal avoidance strategies can be determined. However, in some special scenarios, such as space debris capture, not only is the computational cost large, but also the value of collision probability exceeds the tolerance threshold (Sun et al., 2014). Therefore, the application of the collision probability is limited in these scenarios.

To address this problem, Wang et al. (2017; 2018) proposed an Equal-Collision-Probability-Curve (ECPC) method for the spacecraft close-range safe proximity problem in the presence of navigation and control uncertainties. Firstly, considering those uncertainties, the ECPC around the chief spacecraft is established. Then, a novel auxiliary function is proposed to calculate the gradient direction of the traditional collision probability function. Along with the estimated gradient direction, a collision avoidance manoeuvre can be executed to guarantee the safety of the mission. The effectiveness of this novel avoidance scheme can be theoretically verified (Ge et al., 2002; Ni et al., 2016). Furthermore, this method requires a low computational burden. In the ECPC method, the geometrical shapes of the two spacecraft are assumed to be spherical. The shapes of most spacecraft are not simple spheres but the geometrical shape has a great influence on the collision potential (Bai et al., 2016). Hence, when only the ECPC method is adopted, the safety performance of the space mission deteriorates.

With the discussion above, a Multi-Equal-Collision-Probability-Curve (MECPC) method is proposed to assist in delivering convex polygon-shape spacecraft close-range safe proximity. First, the convex polygon shape chief spacecraft is divided into several small components and each small component has a minimum exterior envelope. Then, the problem of spacecraft close-range safe proximity in the presence of the convex shape can be decomposed into multiple problems of safe spherical spacecraft close-range proximity. With the divided smaller parts and its corresponding minimum exterior enveloping circle, the ECPC method is used to generate the corresponding avoidance manoeuvres. Finally, the superposition of avoidance manoeuvres with respect to the corresponding small components is taken as the ultimate avoidance manoeuvre. As the deputy spacecraft does not collide with every smaller component, it can be kept away from the chief spacecraft. Moreover, an Improved Linear Quadratic Regulator (ILQR) is designed to track the reference trajectory. Compared with the ECPC method, the MECPC can guarantee safe spacecraft proximity in presence of a chief spacecraft with a convex polygon shape.

This rest of this paper is organised as follows. A linear dynamics of spacecraft relative motion is provided Section 2, followed by a description of the ECPC method in Section 3. The MECPC method in the presence of a convex polygon shape spacecraft is developed in

Section 4. In Section 5, using the MECPC method and the ILQR controller, a composite control law is designed and analysed. Numerical simulations are presented in Section 6, and Section 7 concludes the paper.

2. DYNAMICS OF SPACECRAFT RELATIVE MOTION. This section illustrates the spacecraft relative motion dynamics. The Local Vertical Local Horizontal (LVLH) coordinate (Cao et al., 2014; Ou and Zhang, 2017a) is utilised to describe the spacecraft relative motion. The LVLH coordinate is centred at the centroid of the chief spacecraft, the x -axis points out radially from the centre of the Earth to the mass centre of the chief spacecraft, the y -axis is aligned in the direction of in-track motion and the z -axis completes the right-handed coordinate system. Furthermore, as the in-plane is decoupled from motion normal to the orbital plane, the six-dimensional system can be reduced into a second-order system for the motion normal to the nominal orbit plane and a fourth-order system for the in-plane motion. Then, only the coplanar problem is considered in this paper and hence the relative motion is given as:

$$\begin{cases} \ddot{x}_t - 2n\dot{y}_t - 3n^2x_t = u_{x-t} \\ \ddot{y}_t + 2n\dot{x}_t = u_{y-t} \end{cases} \tag{1}$$

where $\mathbf{r}_{1-t} = [x_t, y_t]^T$ and $\mathbf{v}_{1-t} = [v_{x-t}, v_{y-t}]^T$ represent the relative positions and relative velocities in LVLH coordinates, respectively. $\mathbf{u}_{1-t} = [u_{x-t}, u_{y-t}]^T$ represents the control acceleration, μ is the gravitational constant of the Earth, a represents the semi-major axis of the orbit of the chief spacecraft and n is the angular velocity, where $n = \sqrt{\mu/a^3}$.

Then, the forces along both planar directions are assumed to be independent and we obtain the state dynamics matrix \mathbf{A} and \mathbf{B} , which is shown as:

$$\dot{\mathbf{X}} = \mathbf{A}\mathbf{X} + \mathbf{B}\mathbf{u} \tag{2}$$

where $\mathbf{X} = [\mathbf{r}_{1-t}^T \ \mathbf{v}_{1-t}^T]^T$ is the state vector:

$$\mathbf{A} = \begin{bmatrix} 0 & 0 & 1 & 0 \\ 0 & 0 & 0 & 1 \\ 3n^2 & 0 & 0 & 2n \\ 0 & 0 & -2n & 0 \end{bmatrix}, \mathbf{B} = \begin{bmatrix} 0 & 0 & 1 & 0 \\ 0 & 0 & 0 & 1 \end{bmatrix}^T \tag{3}$$

Furthermore, as only the circular orbit of the chief spacecraft is considered in this paper, we obtain the analytical solution $\mathbf{X}(t)$ as:

$$\mathbf{X}(t) = \Phi(t_0, t)\mathbf{X}(t_0) + \int_{t_0}^t \Phi_v(s, t)\mathbf{u}(s)ds \tag{4}$$

where t_0 is the initial time and the transition matrix $\Phi(t_0, t)$ is given by:

$$\Phi(t_0, t) = \begin{bmatrix} \Phi_{rr}(t_0, t) & \Phi_{rv}(t_0, t) \\ \Phi_{vr}(t_0, t) & \Phi_{vv}(t_0, t) \end{bmatrix}, \Phi_v(t_0, t) = \begin{bmatrix} \Phi_{rv}(t_0, t) \\ \Phi_{vv}(t_0, t) \end{bmatrix} \tag{5}$$

where $\Phi_{rr}(t_0, t)$, $\Phi_{rv}(t_0, t)$, $\Phi_{vr}(t_0, t)$, $\Phi_{vv}(t_0, t)$ are obtained as follows:

$$\begin{aligned} \Phi_{rr}(t_0, t) &= \begin{bmatrix} 4 - 3 \cos(n(t - t_0)) & 0 \\ 6(\sin(n(t - t_0)) - n(t - t_0)) & 1 \end{bmatrix}, \\ \Phi_{rv}(t_0, t) &= \frac{1}{n} \begin{bmatrix} \sin(n(t - t_0)) & 2(1 - \cos(n(t - t_0))) \\ -2(1 - \cos(n(t - t_0))) & 4 \sin(n(t - t_0)) - 3n(t - t_0) \end{bmatrix}, \\ \Phi_{vr}(t_0, t) &= \begin{bmatrix} 3n \sin(n(t - t_0)) & 0 \\ 6n(\cos(n(t - t_0)) - 1) & 0 \end{bmatrix}, \\ \Phi_{vv}(t_0, t) &= \begin{bmatrix} \cos(n(t - t_0)) & 2 \sin(n(t - t_0)) \\ -2 \sin(n(t - t_0)) & 4 \cos(n(t - t_0)) - 3 \end{bmatrix}. \end{aligned} \tag{6}$$

3. THE ECPC METHOD. Wang et al. (2017; 2018) developed an ECPC method for spacecraft close-range safe proximity in the presence of uncertainties. Similar to the concept of an isobaric curve, the ECPC represents a curve consisting of equal collision probability points around the chief spacecraft. This proposed safe close-range proximity scheme is attractive for two reasons. First, the ECPC method does not need to solve the transcendental function after the approximate treatment, so that the computational burden can be greatly decreased while maintaining the necessary accuracy. More importantly, the effectiveness of the proposed method can be theoretically verified.

Considering the navigation and the control uncertainties, the linear covariance method is utilised to propagate the uncertainties and we obtain the covariance matrix with respect to the state error, which is given as (Yang et al., 2016; Luo and Yang, 2017):

$$\delta X = X - E(X) \tag{7}$$

$$\begin{aligned} C_{\delta X} &= E \{ [\delta X - E(\delta X)][\delta X - E(\delta X)]^T \} \\ &= \Phi(t_0, t) C_{\delta X_0} \Phi(t_0, t)^T + \sum_{i=1}^N \Phi_v(t_i, t) C_{\delta v_i} \Phi_v(t_i, t)^T \end{aligned} \tag{8}$$

where N is the number of control impulses, δX is the error of the X , and $E(X)$ and $E(\delta X)$ represent the mean values of X and δX , respectively. $C_{\delta X_0}$ and $C_{\delta v_i}$ are the covariance matrices of the initial navigation and control uncertainties in LVLH coordinates, respectively and $C_{\delta X}$ is the uncertainty covariance matrix of the state vector.

Wang et al. (2017) developed an equal collision probability cure, which is a Gaussian form and can be described as follows:

$$\begin{cases} \text{if } \frac{x_{1-t}^2}{\sigma_{x-t}^2} + \frac{y_{1-t}^2}{\sigma_{y-t}^2} < D_0 \ \& \ v_{1-t}^{paral} > 0 \\ V_0(\mathbf{r}_{1-t}) = \lambda_0 \left\{ \exp \left[-\frac{1}{2} \left(\frac{x_{1-t}^2}{\sigma_{x-t}^2} + \frac{y_{1-t}^2}{\sigma_{y-t}^2} \right) \right] - \exp \left(-\frac{1}{2} D_0^2 \right) \right\}, \\ \text{else} \\ V_0(\mathbf{r}_{1-t}) = 0. \end{cases} \tag{9}$$

where $C_{\delta r_{1-t}} = \text{diag}([\sigma_{x-t}^2 \ \sigma_{y-t}^2])$ is the uncertainty covariance matrix of the relative position. λ_0 is a positive constant that shapes the repulsive potential magnitude, D_0 is the radius

of the hazardous zone and $v_{1-t}^{parallel}$ is the value of relative parallel velocity, which is given as:

$$v_{1-t}^{parallel} = v_{1-t} \cdot n_{1-t}^{parallel} \tag{10}$$

where $n_{1-t}^{parallel}$ is the unit vector pointing from the deputy spacecraft to the chief spacecraft and $n_{1-t}^{parallel} = -r_{1-t}/|r_{1-t}|$. If $v_{1-t}^{parallel} \leq 0$, the deputy spacecraft is moving away from the chief spacecraft and we do not execute the avoidance manoeuvres. Otherwise, the deputy spacecraft is moving toward the chief spacecraft and the avoidance manoeuvres are implemented.

The hazardous zone is defined as the zone where a collision is likely to happen. Furthermore, the hazardous zone is a sphere around the chief spacecraft and has the following radius:

$$D_0 = d_0(R_0 + D_s) \tag{11}$$

where d_0 is a positive constant and D_s is defined as the braking distance taken to stop once the avoidance manoeuvres are implemented and is computed by:

$$D_s = \frac{(v_{1-t}^{parallel})^2}{2a_{max}} \tag{12}$$

where a_{max} is the maximum control acceleration of the deputy spacecraft. The perpendicular relative velocity of the deputy spacecraft is obtained from:

$$v_{1-t}^{perpen} n_{1-t}^{perpen} = v_{1-t} - v_{1-t}^{parallel} n_{1-t}^{parallel} \tag{13}$$

where v_{1-t}^{perpen} is the value of the perpendicular relative velocity and n_{1-t}^{perpen} is the unit vector perpendicular to $n_{1-t}^{parallel}$, which is as follows:

$$n_{1-t}^{perpen} = -\frac{1}{\sqrt{x_{1-t}^2 + y_{1-t}^2}} \begin{bmatrix} -y_{1-t} \\ x_{1-t} \end{bmatrix} \tag{14}$$

According to Equation (9), we define the negative gradient of the repulsive potential with respect to the position terms as the avoidance manoeuvres (Ge and Cui, 2002):

$$F_{repel} = -\nabla_{r_{1-t}} V_0(r_{1-t}) \tag{15}$$

where:

$$\nabla_{r_{1-t}} V_0(r_{1-t}) = \frac{\partial V_0(r_{1-t})}{\partial r_{1-t}} \frac{\partial r_{1-t}}{\partial r_{1-t}} + \frac{\partial V_0(r_{1-t})}{\partial D_0} \frac{\partial D_0}{\partial r_{1-t}} \tag{16}$$

With the help of Equations (9), (15) and (16), we obtain the collision avoidance manoeuvre as:

$$F_{repel} = F_{oparal} + F_{perpen} \tag{17}$$

where

$$M_1 = \exp \left[-\frac{1}{2} \left(\frac{x_{1-t}^2}{\sigma_{x-t}^2} + \frac{y_{1-t}^2}{\sigma_{y-t}^2} \right) \right], M_2 = \exp \left(-\frac{1}{2} D_0^2 \right) \tag{18}$$

$$F_{oparal} = -\lambda_0 r_{1-t} M_1 \left(\frac{1}{\sigma_{x-t}^2} + \frac{1}{\sigma_{y-t}^2} \right) n_{1-t}^{parallel}, F_{perpen} = \lambda_0 D_0 M_2 d_0 \frac{v_{1-t}^{parallel}}{a_{max}} \frac{v_{1-t}^{perpen}}{r_{1-t}} n_{1-t}^{perpen} \tag{19}$$

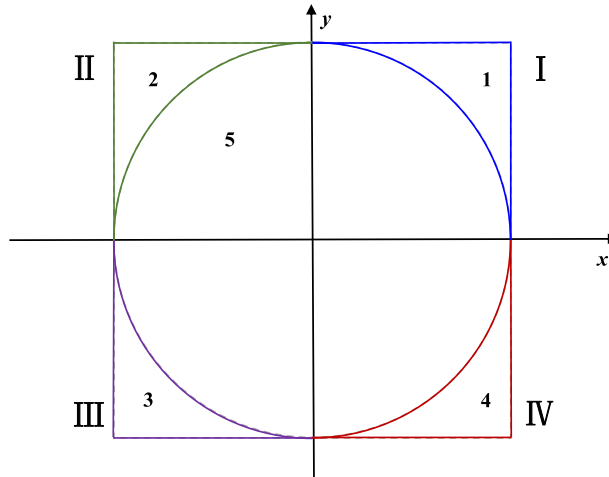


Figure 1. The defined divisions of the convex polygon shape chief spacecraft.

4. THE MECPC METHOD. As the collision probability varies with different shapes (Bai et al., 2016), the shape has great influence on the traditional ECPC method. However, in the ECPC method, Wang et al. (2017; 2018) assumed that the geometrical shapes of the two spacecraft were spheres but most space objects are not actually spheres. Therefore, if the spacecraft shape is assumed as a sphere in some scenarios, the safety performance of the mission deteriorates, as a collision will normally lead to mission failure. To address this problem, the MECPC method is proposed to guarantee convex polygon shape spacecraft safe proximity with other spacecraft.

Assuming that the shape of the chief spacecraft is a convex polygon, such as a square, the chief spacecraft's geometrical shape can be divided into one maximum inside envelope circle part and several arbitrary parts. Moreover, each arbitrary shape part has its corresponding minimum exterior envelope circle. Once the deputy spacecraft flies around the chief spacecraft, the function modules, which are the maximum inside the envelope circle part with respect to the main circle and the minimum exterior envelope circle part with respect to the arbitrary shape parts, jointly generate avoidance manoeuvres on the deputy spacecraft with the basic ECPC method. Figure 1 shows the defined divisions of the convex polygon shape chief spacecraft. As shown in Figure 1, the vertical coordinates system is divided into parts I II, III and IV. The convex polygon shape of the chief spacecraft is also separated into five parts, and part 5 is the maximum inside envelope circle. When the deputy spacecraft flies around the chief spacecraft, the function module is selected by:

$$\begin{cases} \text{Part 1 and Part 5, } h = 1 & x > 0 \text{ and } y > 0 \\ \text{Part 2 and Part 5, } h = 2 & x < 0 \text{ and } y > 0 \\ \text{Part 3 and Part 5, } h = 3 & x < 0 \text{ and } y < 0 \\ \text{Part 4 and Part 5, } h = 4 & x > 0 \text{ and } y < 0 \\ \text{Part 5, } h = 5 & x = 0 \text{ or } y = 0 \end{cases} \quad (20)$$

The transformation from the $O_{1x_1y_1}$ frame to the $O_{1x_{1d}y_{1d}}$ frame in which $C_{\delta r_{10-t}}$ is diagonalized is given by $G_{1-t}W_1^{-1}$:

$$C_{\delta r_{10-t}} = G_{1-t}W_1^{-1}C_{\delta r_{10-t}}(G_{1-t}W_1)^{-1} = \begin{bmatrix} \sigma_{x-t}^2 & 0 \\ 0 & \sigma_{y-t}^2 \end{bmatrix} \tag{25}$$

where G_{1-t} is an orthogonal transformation.

According to Equations (21), (23) and (25), the relative position and relative velocity in the $O_{1x_{1d}y_{1d}}$ coordinates are given as:

$$r_{10-td} = G_{1-t} \{ r_{1-t} - [x_{10} \quad y_{10}]^T \}, v_{10-td} = G_{1-t}v_{1-t} \tag{26}$$

where $r_{10-td} = [x_{10-td}, y_{10-td}]^T$ and $v_{10-td} = [v_{x_{10-td}}, v_{y_{10-td}}]^T$ represent the relative position and the relative velocity in the $O_{1x_{1d}y_{1d}}$ coordinates, respectively.

From Equations (9)–(26), when the deputy spacecraft flies in Section I, the collision avoidance manoeuvres generated by Part 1 in the LVLH coordinates are given as:

$$F_{10-repel} = F_{10-para} + F_{10-perpen} \tag{27}$$

where D_{010} is radius of the hazardous zone around Part 1 in the $O_{1x_{1d}y_{1d}}$ coordinates. r_{10-td} is the value of relative position in the $O_{1x_{1d}y_{1d}}$ coordinates, v_{10-td}^{para} and v_{10-td}^{perpen} are the value of relative parallel velocity and relative perpendicular velocity in the $O_{1x_{1d}y_{1d}}$ coordinates and n_{10-td}^{para} and n_{10-td}^{perpen} represent the unit vector opposite and perpendicular to r_{1-td} , respectively.

$$M_{110d} = \exp \left[-\frac{1}{2} \left(\frac{x_{10-td}^2}{\sigma_{x-t}^2} + \frac{y_{10-td}^2}{\sigma_{y-t}^2} \right) \right], M_{210d} = \exp \left(-\frac{1}{2} D_{010}^2 \right) \tag{28}$$

$$F_{10-para} = -\lambda_0 r_{1-td} M_{110d} \left(\frac{1}{\sigma_{x-t}^2} + \frac{1}{\sigma_{y-t}^2} \right) n_{10-td}^{para} \tag{29}$$

$$F_{10-perpen} = \lambda_0 D_{010} M_{210d} d_0 \frac{v_{10-td}^{para}}{a_{max}} \frac{v_{10-td}^{perpen}}{r_{10-td}} n_{10-td}^{perpen} \tag{30}$$

With the aid of Equations (9), (10), (14) and Equations (21)–(22), we obtain:

$$r_{10} = a_{10-1} n_{1-t}^{para} + a_{10-2} n_{1-t}^{perpen} \tag{31}$$

where:

$$a_{10-1} = -\frac{x_{10}x_{1-t} + y_{10}y_{1-t}}{\sqrt{x_{1-t}^2 + y_{1-t}^2}}, a_{10-2} = \frac{x_{10}y_{1-t} - y_{10}x_{1-t}}{\sqrt{x_{1-t}^2 + y_{1-t}^2}} \tag{32}$$

According to Equations (9)–(32), we obtain:

$$n_{10-td}^{para} = \frac{r_{1-t} + a_{10-1}}{r_{10-td}} n_{1-td}^{para} + \frac{a_{10-2}}{r_{10-td}} n_{1-td}^{perpen} \tag{33}$$

Based on Equation (33), we have

$$n_{10-td}^{perpen} = \frac{a_{10-2}}{+} r_{10-td} n_{1-td}^{para} + \frac{r_{1-t} + a_{10-1}}{r_{10-td}} n_{1-td}^{perpen} \tag{34}$$

From Equations (33) and (34), we obtain:

$$F_{10-para} = - \left[\begin{array}{l} \lambda_0 r_{10-td} M_{110d} \left(\frac{1}{\sigma_{x-td}^2} + \frac{1}{\sigma_{y-td}^2} \right) \frac{r_{1-t} + a_{10-1}}{r_{10-td}} \\ + \lambda_0 D_{010d} M_{210d} d_0 \frac{v_{10-td}^{para} v_{10-td}^{perpen}}{a_{max} r_{10-td} r_{10-td}} \frac{a_{10-2}}{r_{10-td}} \end{array} \right] n_{1-td}^{para} \tag{35}$$

$$F_{10-perpen} = \left[\begin{array}{l} \lambda_0 r_{10-td} M_{110d} \left(\frac{1}{\sigma_{x-td}^2} + \frac{1}{\sigma_{y-td}^2} \right) \frac{a_{10-2}}{r_{10-td}} \\ + \lambda_0 D_{010d} M_{210d} d_0 \frac{v_{10-td}^{para} v_{10-td}^{perpen}}{a_{max} r_{10-td} r_{10-td}} \frac{r_{1-t} + a_{10-1}}{r_{10-td}} \end{array} \right] n_{1-td}^{perpen} \tag{36}$$

According to the above deduction, the collision avoidance manoeuvres generated by Part 2, Part 3 and Part 4 with respect to Section II, Section III and Section IV are given as:

$$F_{i0-repel} = F_{i0-para} + F_{i0-perpen}, (i = 2, 3, 4) \tag{37}$$

where $F_{i0-repel}(i = 2, 3, 4)$ represents the collision avoidance manoeuvres generated by Part 2, Part 3 and Part 4. $r_{i0} = [x_{i0} \ y_{i0}]^T, (i = 2, 3, 4)$ represents the different relative position of the minimum exterior circle's centre with respect to the corresponding part. $r_{i0-td} = [x_{i0-td}, y_{i0-td}]^T$ and $v_{i0-td} = [v_{xi0-td}, v_{yi0-td}]^T (i = 2, 3, 4)$ represent the relative position and the relative velocity in the corresponding coordinates, respectively. $D_{0i0}, (i = 2, 3, 4)$ represents the radius of the corresponding hazardous zones, $r_{i0-td}, (i = 2, 3, 4)$ are values of relative positions in the corresponding coordinates and $v_{i0-td}^{para}, (i = 2, 3, 4)$ and $v_{i0-td}^{perpen}, (i = 2, 3, 4)$ are the values of relative parallel velocity and relative perpendicular velocity in the corresponding coordinates.

$$r_{i0-td} = G_{1-t} \{ r_{1-t} - [x_{i0} \ y_{i0}]^T \}, v_{i0-td} = G_{1-t} v_{1-t}, (i = 2, 3, 4) \tag{38}$$

$$M_{1i0d} = \exp \left[-\frac{1}{2} \left(\frac{x_{i0-td}^2}{\sigma_{x-td}^2} + \frac{y_{i0-td}^2}{\sigma_{y-td}^2} \right) \right], M_{2i0d} = \exp \left(-\frac{1}{2} D_{0i0d}^2 \right), (i = 2, 3, 4) \tag{39}$$

$$a_{i0-1} = -\frac{x_{i0}x_{1-t} + y_{i0}y_{1-t}}{\sqrt{x_{1-t}^2 + y_{1-t}^2}}, a_{i0-2} = -\frac{x_{i0}y_{1-t} + y_{i0}x_{1-t}}{\sqrt{x_{1-t}^2 + y_{1-t}^2}}, (i = 2, 3, 4) \tag{40}$$

$$F_{10-para} = - \left[\begin{array}{l} \lambda_0 r_{i0-td} M_{1i0d} \left(\frac{1}{\sigma_{x-td}^2} + \frac{1}{\sigma_{y-td}^2} \right) \frac{r_{1-t} + a_{i0-1}}{r_{i0-td}} \\ + \lambda_0 D_{0i0d} M_{2i0d} d_0 \frac{v_{i0-td}^{para} v_{i0-td}^{perpen}}{a_{max} r_{i0-td} r_{i0-td}} \frac{a_{i0-2}}{r_{i0-td}} \end{array} \right] n_{1-td}^{para}, (i = 2, 3, 4) \tag{41}$$

$$F_{10-perpen} = - \left[\begin{array}{l} \lambda_0 r_{i0-td} M_{1i0d} \left(\frac{1}{\sigma_{x-td}^2} + \frac{1}{\sigma_{y-td}^2} \right) \frac{a_{i0-2}}{r_{i0-td}} \\ + \lambda_0 D_{0i0d} M_{2i0d} d_0 \frac{v_{i0-td}^{para} v_{i0-td}^{perpen}}{a_{max} r_{i0-td} r_{i0-td}} \frac{r_{1-t} + a_{i0-1}}{r_{i0-td}} \end{array} \right] n_{1-td}^{perpen}, (i = 2, 3, 4) \tag{42}$$

From Equations (9)–(19), the collision avoidance manoeuvres generated by part 5 are given as follows:

$$F_{50-repel} = F_{50-para} + F_{50-perpen} \tag{43}$$

where $F_{50-repel}$ represents the collision avoidance manoeuvres generated by part 5. $r_{50-td} = [x_{50-td}, y_{50-td}]^T$ and $v_{50-td} = [v_{x50-td}, v_{y50-td}]^T$ represent the relative position and the relative velocity in the $O_1x_1y_1$ coordinates, respectively. D_{050} is the radius of the corresponding hazardous zone, r_{50-td} is the value of the relative positions and v_{50-td}^{para} and v_{50-td}^{perpen} are the values of the relative parallel velocity and relative perpendicular velocity in the $O_1x_1y_1$ coordinates.

$$r_{50-td} = G_{1-t}r_{1-t}, v_{50-td} = G_{1-t}v_{1-t} \tag{44}$$

$$M_{150d} = \exp \left[-\frac{1}{2} \left(\frac{x_{50-td}^2}{\sigma_{x-td}^2} + \frac{y_{50-td}^2}{\sigma_{y-td}^2} \right) \right], M_{250d} = \exp \left(-\frac{1}{2} D_{050}^2 \right) \tag{45}$$

$$F_{50-para} = -\lambda_0 r_{50-td} M_{150d} \left(\frac{1}{\sigma_{x-td}^2} \frac{1}{\sigma_{y-td}^2} \right) n_{1-td}^{para} \tag{46}$$

$$F_{50-perpen} = -\lambda_0 D_{050-td} M_{250d} d_0 \frac{v_{50-td}^{para} v_{50-td}^{perpen}}{a_{max} r_{50-td}} n_{1-td}^{perpen} \tag{47}$$

Thus, the total collision avoidance manoeuvres generated are given as:

$$F_{Total-repel} = \begin{cases} F_{50-repel} + F_{h0-repel}, & h = 1, 2, 3, 4 \\ F_{50-repel}, & h = 5 \end{cases} \tag{48}$$

(ii) $x_{ep} \neq 0$ and $y_{ep} \neq 0$

Figure 3 illustrates the force analysis of the deputy spacecraft in Section I. As we can see from Figure 3, part 5 generates force $F_{50-repel}$. By the encounter point r_{ep} , part 1 is divided into two parts, and each part has its own minimum exterior envelope circle. Subsequently, the $O_{1-i}x_{1-i}y_{1-i}$ ($i = 1, 2$) coordinates are established, which have their x_{1-i} axis pointing out from the origin in the LVLH coordinates toward the centre of the minimum exterior envelope circle located at the centre. The y_{1-i} axis of the $O_{1-i}x_{1-i}y_{1-i}$ ($i = 1, 2$) frame has the same direction as the x_{1-i} axis and is rotated 90° counter-clock-wise along the Oz axis.

In this section, the following condition is divided into the following four parts:

$$\begin{cases} h_1 = 1 & x_{ep} > 0 \text{ and } y_{ep} > 0 \\ h_1 = 2 & x_{ep} < 0 \text{ and } y_{ep} > 0 \\ h_1 = 3 & x_{ep} < 0 \text{ and } y_{ep} < 0 \\ h_1 = 4 & x_{ep} > 0 \text{ and } y_{ep} < 0 \end{cases} \tag{49}$$

If the condition $h_1 = 1$ is satisfied, Figure 3 illustrates the force analysis of the deputy spacecraft in Section I. From Figure 3, the minimum exterior envelope circle of part 1-1 and part 1-2 generate the repulsive force $F_{11-repel}$ and $F_{12-repel}$, respectively. Furthermore, both the $O_{1-1}x_{1-1}y_{1-1}$ coordinates and the $O_{1-2}x_{1-2}y_{1-2}$ coordinates are established as the $O_1x_1y_1$ coordinates depicted in Figure 2.

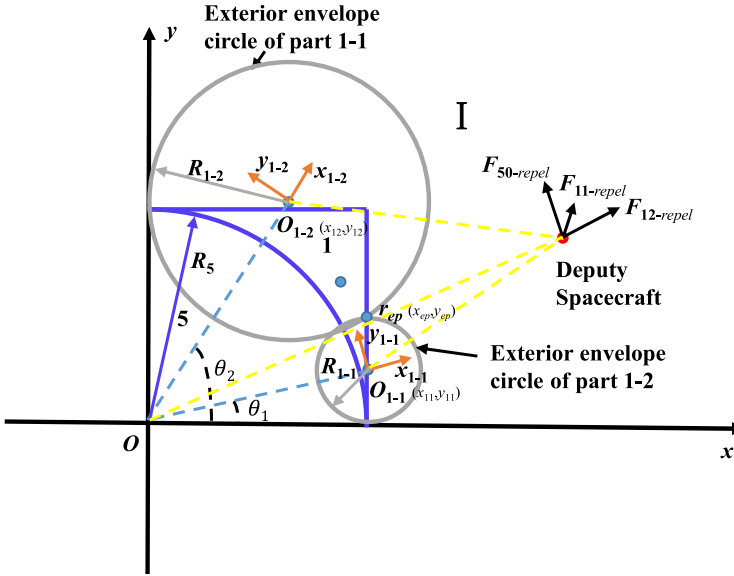


Figure 3. The force analysis of the deputy spacecraft in Section I and the condition $h_1 = 1$.

From Equations (9)–(36), the collision avoidance manoeuvres generated with respect to the corresponding part are given as:

$$F_{ij-repel} = F_{ij-para} + F_{ij-perpen} (i = 1, 2, 3, 4, j = 1, 2) \tag{50}$$

where $F_{ij-repel} (i = 1, 2, 3, 4, j = 1, 2)$ represent the collision avoidance manoeuvres generated by the corresponding part. $r_{ij} = [x_{ij} \ y_{ij}]^T, (i = 1, 2, 3, 4, j = 1, 2)$ represent the different relative position of the minimum exterior circle’s centre with respect to the corresponding part. $r_{ij-td} = [x_{ij-td} \ y_{ij-td}]^T, v_{ij-td} = [v_{xij-td} \ v_{yij-td}]^T (i = 1, 2, 3, 4, j = 1, 2)$ represent the relative position and the relative velocity in the corresponding coordinates, respectively. $D_{0ij}, (i = 1, 2, 3, 4, j = 1, 2)$ are the radii of the corresponding hazardous regions, $r_{ij-td}, (i = 1, 2, 3, 4, j = 1, 2)$ are values of relative positions in the corresponding coordinates and $v_{ij-td}^{para}, (i = 1, 2, 3, 4, j = 1, 2)$ and $v_{ij-td}^{perpen}, (i = 1, 2, 3, 4, j = 1, 2)$ are the values of relative parallel velocity and relative perpendicular velocity in the corresponding coordinates.

$$r_{ij-td} = G_{1-t} \{ r_{1-t} - [x_{ij} \ y_{ij}]^T \}, v_{ij-td} = G_{1-t} v_{1-t}, (i = 1, 2, 3, 4, j = 1, 2) \tag{51}$$

$$M_{1ijd} = \exp \left[-\frac{1}{2} \left(\frac{x_{ij-td}^2}{\sigma_{x-td}^2} + \frac{y_{ij-td}^2}{\sigma_{y-td}^2} \right) \right], M_{2ijd} = \exp \left(-\frac{1}{2} D_{0ijd}^2 \right) (i = 1, 2, 3, 4, j = 1, 2) \tag{52}$$

$$a_{ij-1} = -\frac{x_{ij}x_{1-t} + y_{ij}y_{1-t}}{\sqrt{x_{1-t}^2 + y_{1-t}^2}}, a_{ij-2} = -\frac{x_{ij}y_{1-t} + y_{ij}x_{1-t}}{\sqrt{x_{1-t}^2 + y_{1-t}^2}}, (i = 1, 2, 3, 4, j = 1, 2) \tag{53}$$

$$F_{ij-parallel} = - \left[\begin{array}{l} \lambda_0 r_{ij-td} M_{1ijd} \left(\frac{1}{\sigma_{x-td}^2} + \frac{1}{\sigma_{y-td}^2} \right) \frac{r_{1-t} + a_{ij-1}}{r_{ij-td}} \\ + \lambda_0 D_{0ijd} M_{2ijd} d_0 \frac{v_{ij-td}^{parallel} v_{ij-td}^{perpen}}{a_{max} r_{ij-td} r_{ij-td}} \frac{a_{ij-2}}{r_{ij-td}} \end{array} \right] n_{1-t}^{parallel}, (i = 1, 2, 3, 4, j = 1, 2) \tag{54}$$

$$F_{ij-perpen} = - \left[\begin{array}{l} -\lambda_0 r_{ij-td} M_{1ijd} \left(\frac{1}{\sigma_{x-td}^2} + \frac{1}{\sigma_{y-td}^2} \right) \frac{a_{ij-2}}{r_{ij-td}} \\ + \lambda_0 D_{0ijd} M_{2ijd} d_0 \frac{v_{ij-td}^{parallel} v_{ij-td}^{perpen}}{a_{max} r_{ij-td} r_{ij-td}} \frac{r_{1-t} + a_{ij-1}}{r_{ij-td}} \end{array} \right] n_{1-t}^{perpen}, (i = 1, 2, 3, 4, j = 1, 2). \tag{55}$$

Thus, the total collision avoidance manoeuvres are obtained as:

$$F_{Total-repel} = \begin{cases} F_{50-repel} + F_{h1-repel} + F_{h2-repel}, & h = h_1 \\ F_{50-repel} + F_{h0-repel} & h = 1, 2, 3, 4 \text{ \& } h \neq h_1. \\ F_{50-repel} & h = 5 \end{cases} \tag{56}$$

5. THE EFFECTIVE COLLISION AVOIDANCE CONTROL LAW AND THE DEFINITION OF THE COMPOSITE CONTROL LAW. If $x_{1-t}^2/\sigma_{x-t}^2 + y_{1-t}^2/\sigma_{y-t}^2 < D_0$, the relative parallel velocity $v_{1-t}^{parallel} > 0$ at any time t and $\forall |r_{1-t}| \neq 0$ are satisfied and the repulsive force is activated. In this section, we analyse the effectiveness of the avoidance scheme and design the composite law.

5.1. Analysis of the effective collision avoidance control law. According to Equations (9)–(56), the following conditions are satisfied:

- 1) $M_{1ijd} > M_{2ijd} > 0 (i = 1, 2, 3, 4, j = 0, 1, 2), M_{150d} > M_{250d} > 0.$
- 2) $\lambda_0 > 0, D_{0ijd} > R_0 > 0 (i = 1, 2, 3, 4, j = 0, 1, 2), D_{050d} > R_0 > 0.$
- 3) $d_0 > 0, a_{max} > 0, r_{ij-td} > 0 (i = 1, 2, 3, 4, j = 0, 1, 2), r_{50-td} > 0.$
- 4) $v_{ij-td}^{parallel} > 0, v_{ij-td}^{perpen} > 0 (i = 1, 2, 3, 4, j = 0, 1, 2), v_{50-td}^{parallel} > 0, v_{50-td}^{perpen} > 0.$

As the parallel repulsive force is much larger than the perpendicular repulsive force (Ge and Cui, 2002), we get

$$\lambda_0 r_{ij-td} M_{1ijd} \left(\frac{1}{\sigma_{x-t}^2} + \frac{1}{\sigma_{y-t}^2} \right) \gg \lambda_0 D_{0ijd} M_{2ijd} d_0 \frac{v_{ij-d}^{parallel} v_{ij-d}^{perpen}}{a_{max} r_{ij-d}} > 0 (i = 1, 2, 3, 4, j = 0, 1, 2) \tag{57}$$

$$\lambda_0 r_{50-td} M_{150-td} \left(\frac{1}{\sigma_{x-t}^2} + \frac{1}{\sigma_{y-t}^2} \right) \gg \lambda_0 D_{050d} M_{250-td} d_0 \frac{v_{50-d}^{parallel} v_{50-d}^{perpen}}{a_{max} r_{50-td}} > 0 \tag{58}$$

Subsequently, from Equations (48) and (56), we obtain the total collision avoidance manoeuvres as follows:

$$F_{Total-repel} = F_{Total-parallel} + F_{Total-perpen} \tag{59}$$

where:

$$F_{Total-parallel} = \begin{cases} x_{ep} = 0 \text{ or } y_{ep} = 0 & \begin{cases} F_{50-parallel} + F_{h0-parallel}, & h = 1, 2, 3, 4 \\ F_{50-parallel}, & h = 5 \end{cases} \\ x_{ep} \neq 0 \text{ and } y_{ep} \neq 0 & \begin{cases} F_{50-parallel} + F_{h1-parallel} + F_{h2-parallel}, & h = h_1 \\ F_{50-parallel} + F_{h0-parallel}, & h = 1, 2, 3, 4 \text{ \& } h \neq h_1 \\ F_{50-parallel}, & h = 5 \end{cases} \end{cases} \tag{60}$$

$$F_{Total-perpen} = \begin{cases} x_{ep} = 0 \text{ or } y_{ep} = 0 & \begin{cases} F_{50-perpen} + F_{h0-perpen}, & h = 1, 2, 3, 4 \\ F_{50-perpen}, & h = 5 \end{cases} \\ x_{ep} \neq 0 \text{ and } y_{ep} \neq 0 & \begin{cases} F_{50-perpen} + F_{h1-perpen} + F_{h2-perpen}, & h = h_1 \\ F_{50-perpen} + F_{h0-perpen}, & h = 1, 2, 3, 4 \text{ \& } h \neq h_1 \\ F_{50-perpen}, & h = 5 \end{cases} \end{cases} \tag{61}$$

Therefore, based on Equations (57) and (58), the parallel force $F_{Total-parallel}$ is along the negative direction of $n_{1-t}^{parallel}$ and prevents the deputy spacecraft from moving closer to the chief spacecraft. The perpendicular component $F_{Total-operpen}$ of the force $F_{Total-repel}$ steers the deputy spacecraft around the chief spacecraft.

As the parallel repulsive force is much larger than the perpendicular repulsive force (Ge and Cui, 2002), therefore, the main analysis of the repulsive force is with respect to the parallel repulsive force. Moreover, as the force $F_{Total-repel}$ contains the force $F_{50-parallel}$ in every condition, $F_{50-parallel}$ can be taken as an example to show the analysis progress in proving the effectiveness of the MECPC method. Subsequently, the parallel repulsive force generated by part 5 is differentiated with respect to the relative distance as:

$$\frac{\partial F_{50-parallel}}{\partial r_{50-td}} = -\lambda_0 M_{150d} \left(\frac{1}{\sigma_{x-td}^2} + \frac{1}{\sigma_{y-td}^2} \right)^2 r_{50-td}^2 + \lambda_0 M_{150d} \left(\frac{1}{\sigma_{x-td}^2} + \frac{1}{\sigma_{y-td}^2} \right). \tag{62}$$

Similar to Equation (62), the auxiliary function I with respect to $h(r_{50-td})$ is defined as:

$$h(r_{50-td}) = -\lambda_0 M_{150d} \left(\frac{1}{\sigma_{x-td}^2} + \frac{1}{\sigma_{y-td}^2} \right)^2 r_{50-td}^2 + \lambda_0 M_{150d} \left(\frac{1}{\sigma_{x-td}^2} + \frac{1}{\sigma_{y-td}^2} \right). \tag{63}$$

With the help of Equation (63), the defined auxiliary function is a second-order equation with respect to r_{50-td} and its quadratic coefficient is negative. Therefore, the maximum value of Equation (63) can be obtained as:

$$H_{max}(r_{50-td}) = \lambda_0 M_{150d} \left(\frac{1}{\sigma_{x-td}^2} + \frac{1}{\sigma_{y-td}^2} \right) > 0. \tag{64}$$

Equation (63) has two zero points and its symmetry axis is zero. Moreover, we have $r_{50-td} > 0$. Then, $x_2 > 0$ is assumed to be one zero point with respect to $h(r_{50-td})$, which is

given as:

$$X_2 = \frac{\sigma_{x-td}\sigma_{y-td}}{\sqrt{\sigma_{x-td}^2 + \sigma_{y-td}^2}} \tag{65}$$

As a result, if $r_{50-td} > x_2, h(r_{50-td}) < 0$, if $0 < r_{50-td} < x_2, h(r_{50-td}) > 0$.

From Equation (9), x_3 is assumed to be the maximum value of r_{50-td} , which is defined as:

$$r_{50-td} < x_3 = \max \left(\sqrt{\sigma_{y-t}^2 D_{050} + x_{1-t}^2 \left(1 - \frac{\sigma_{y-t}^2}{\sigma_{x-t}^2}\right)}, \sqrt{\sigma_{y-t}^2 D_{050} + x_{1-t}^2 \left(1 - \frac{\sigma_{y-t}^2}{\sigma_{x-t}^2}\right)} \right) \tag{66}$$

According to Equations (62)–(66), if $x_2 < r_{50-td} < x_3, \partial F_{50-parallel} / \partial r_{50-td} < 0$. Moreover, $F_{50-parallel}$ is a decreasing function; if $0 < r_{50-td} < x_2, \partial F_{50-parallel} / \partial r_{50-td} > 0$. $F_{50-parallel}$ is an increasing function. Then, the critical point ζ_{50} is the minimum relative distance between the deputy spacecraft and the centre of part 5 of the chief spacecraft and thus we obtain the critical point. When the deputy spacecraft reaches the critical point ζ_{50} , its parallel relative velocity decreases to zero.

According to the above analysis, the critical points $\zeta_{ij} (i = 1, 2, 3, 4, j = 0, 1, 2)$ and ζ_{50} with respect to those parts can be obtained. Figure 4 shows the interval of speed range in the collision avoidance manoeuvre in two conditions. Using the available parameters' values $\{\lambda_0, d_0\}$, the deputy spacecraft will not collide with the chief spacecraft when the following condition is satisfied:

$$\begin{cases} \zeta_{50} > R_{50} \ \& \ \zeta_{i0} > R_{i0} (i = 1, 2, 3, 4); \text{ If } x_{ep} = 0 \text{ or } y_{ep} = 0 \\ \zeta_{50} > R_{50} \ \& \ \zeta_{ij} > R_{ij} (i = 1, 2, 3, 4, j = 1, 2); \text{ If } x_{ep} \neq 0 \text{ or } y_{ep} \neq 0 \end{cases} \tag{67}$$

where $R_{ij} (i = 1, 2, 3, 4, j = 0, 1, 2)$ are the radii of the small components' exterior envelope circle. R_{50} is the radius of part 5's exterior envelope circle.

5.2. *The composite control law.* Considering a system as Equation (2), the LQR controller is utilised to find an optimal control law. Furthermore, the cost function (Lin, 2007; Xing et al., 2016) is given as:

$$J_0 = \frac{1}{2} \int_{t_0}^{\infty} [X^T Q X + u^T R u] dt \tag{68}$$

where $Q \geq 0$ and $1 \geq R \geq 0$ are semi-positive definite symmetric matrices. According to the principle of minimum values as per Equation (68), we obtain the optimal control law as follows:

$$u^* = K_1 X \tag{69}$$

where $K_1 = -R^{-1} B^T S_1$ is the optimal feedback gain matrix and S_1 is a matrix which satisfies the Riccati equation:

$$S_1 A + A^T S_1 - S_1 B R^{-1} B^T S_1 + Q = 0. \tag{70}$$

According to Equations (2) and (68), we can obtain $u^*(t)$ by solving the Riccati algebraic equation. Then, the ILQR controller is proposed to track the reference trajectory and introduced below.

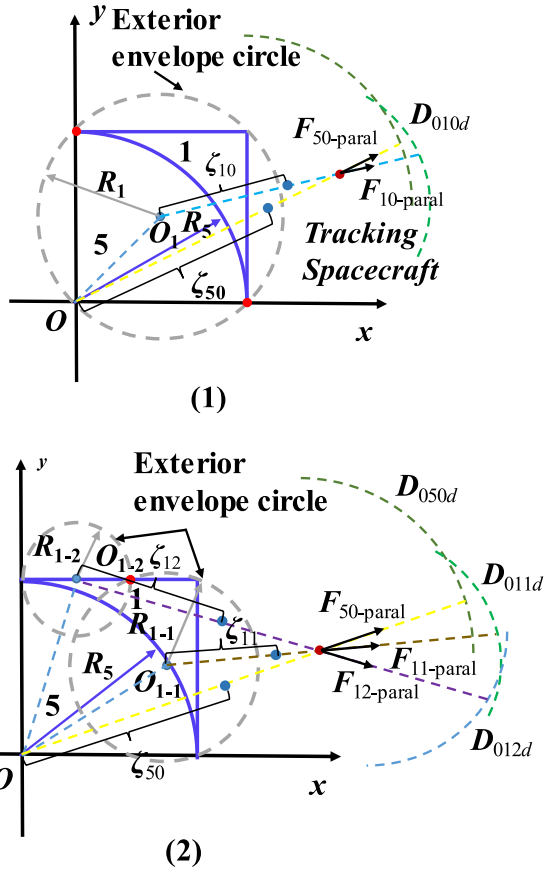


Figure 4. The interval of speed range in collision avoidance manoeuvre in two conditions.

Based on Equation (59), we obtain:

$$F_{Total-repel} = b_{11}n_{1-td}^{parallel} + b_{12}n_{1-td}^{perpen} \tag{71}$$

where b_{11}, b_{12} are the auxiliary parameters.

With the help of Equations (9)–(14), Equation (71) is computed by:

$$F_{Total-repel} = K_2X \tag{72}$$

where:

$$K_2 = \frac{1}{r_{1-t}} \begin{bmatrix} -b_{11} & b_{12} & 0 & 0 \\ -b_{12} & b_{11} & 0 & 0 \end{bmatrix}. \tag{73}$$

From Equation (73), we get:

$$K_2^T K_2 \leq \begin{bmatrix} K_3 & 0_{2 \times 2} \\ 0_{2 \times 2} & 0_{2 \times 2} \end{bmatrix} \tag{74}$$

where:

$$\mathbf{K}_3 = \frac{b_{11}^2 + b_{12}^2}{r_{1-t}^2} \mathbf{I}_{2 \times 2} \quad (75)$$

Furthermore, the upper matrix \mathbf{K}_4 on the $\mathbf{K}_2^T(t)\mathbf{K}_2(t)$ is defined as:

$$\mathbf{K}_4 = \begin{bmatrix} K_{upper} \mathbf{I}_{2 \times 2} & \mathbf{0}_{2 \times 2} \\ \mathbf{0}_{2 \times 2} & \mathbf{0}_{2 \times 2} \end{bmatrix} \quad (76)$$

where:

$$\frac{b_{11}^2 + b_{12}^2}{r^2} \leq K_{upper} \quad (77)$$

Considering a system as Equation (2), the ILQR controller aims to find an optimal control law which minimises the following cost function (Xing et al., 2016):

$$J = \frac{1}{2} \int_{t_0}^{\infty} \left[X^T \left(\frac{\mathbf{K}_4}{m^2} + \mathbf{Q} \right) X + u^T \mathbf{R} u \right] dt \quad (78)$$

where m is the mass of the deputy spacecraft. With the help of the principle of minimum values as per Equation (78), we get the optimal control as:

$$u_1^* = \mathbf{K}_5 X \quad (79)$$

where $\mathbf{K}_5 = -\mathbf{R}^{-1} \mathbf{B}^T \mathbf{S}_2$ is the optimal feedback gain matrix and \mathbf{S}_2 is a matrix which satisfies the Riccati equation:

$$\mathbf{S}_2 \mathbf{A} + \mathbf{A}^T \mathbf{S}_2 - \mathbf{S}_2 \mathbf{B} \mathbf{R}^{-1} \mathbf{B}^T \mathbf{S}_2 + \frac{\mathbf{K}_4}{m^2} + \mathbf{Q} = 0 \quad (80)$$

Based on Equations (2) and (78), the design of u_1^* can be obtained by solving the Riccati algebraic equation. Then, the auxiliary function Π (Lin, 2007) is given as:

$$V_1(X) = \min_{u^*} \int_0^{\infty} \left(X^T \left(\frac{\mathbf{K}_4}{m^2} + \mathbf{Q} \right) X + u^T \mathbf{R} u \right) dt. \quad (81)$$

As the $V_1(X)$ is the minimum cost of the optimal control of the nominal system from some initial state X , $V_1(X)$ is defined as a Lyapunov function of Equation (2). By definition, $V_1(X)$ must satisfy the Hamilton-Jacobi-Bellman equation (Lin, 2007):

$$\min_{u^*} \left\{ X^T \left(\frac{\mathbf{K}_4}{m^2} + \mathbf{Q} \right) X + u^T \mathbf{R} u + V_{1-X}^T (\mathbf{A} X + \mathbf{B} u) \right\} = 0 \quad (82)$$

where $V_{1-X} = (\partial V / \partial X)$. Since $u_1^* = \mathbf{K}_5 X$ is the optimal control, it must satisfy: (1) the above minimum zero; and (2) the derivative of $X^T (\mathbf{K}_4 / m^2 + \mathbf{Q}) X + u^T \mathbf{R} u + V_{1-X}^T (\mathbf{A} X +$

Bu) with respect to u is zero.

$$X^T \left(\frac{K_4}{m^2} + Q \right) X + X^T K_5^T R K_5 X + V_{1-X}^T (AX + BK_5 X) = 0 \tag{83}$$

$$2X^T K_5^T + V_{1-X}^T B = 0. \tag{84}$$

So, the composite controller is given as:

$$u_{total} = u_1^* + \frac{F_{Total-repel}}{m} \tag{85}$$

Based on the Lyapunov-based method, the stability of the overall close-system with the composite controller is verified (Lin, 2007).

5.3. *The flow of the MECPC method algorithm.* With the aid of Equations (2)–(85), we obtain Algorithm 1 to describe the MECPC method. The control error of the deputy spacecraft is assumed to be an uncorrelated zero-mean Gaussian distribution (Psiaki, 2011; Peynot et al., 2014). Furthermore, the covariance matrix of the control uncertainty is given as follows (Luo et al., 2011):

$$C_{\delta\Delta v_t} = \begin{cases} 0, & \text{if } |u| = 0 \\ \text{Diag} \left([(0.02 + 0.01|u_x|)^2, (0.02 + 0.01|u_y|)^2] \right), & \text{if } |u| \neq 0 \end{cases} \tag{86}$$

Algorithm 1. The MECPC method.

Number	Content
1	Initialisation: $X_0, \lambda_0, d_0, R_0, m, a_{max}, t_f, C_{\delta X_0}$.
2	The reference trajectory of the deputy spacecraft is designed, X_p is the reference relative vector and the control impulse u_T is obtained for orbital transformation.
3	Using Equation (2) and Equations (78)–(80), we compute the optimal feedback gain matrix K_5 .
4	For $t = 1, 2, \dots, t_f$, implement the following MECPC steps.
5	The “virtual” actual state vector $X_{a-1}(t)$ is computed by the sum of the actual state vector X_a and navigation uncertainties.
6	Based on Equation (79), we obtain the optimal control impulse u_1^* to track reference trajectory.
7	According to Equation (86), we get the control uncertainty matrix $C_{\delta\Delta v_t}$.
8	Via Equations (7) and (8), we compute the covariance matrix $C_{\delta x}$ of state error.
9	By Equations (9)–(61), the repel force $F_{Total-repel}$ is obtained with $C_{\delta x}$ and $X_{a-1}(t)$.
10	Then, using Equation (85), we compute the u_{Total} .
11	With the aid of the u_{Total} and old X_a , we update the new actual state vector X_a .
12	End

6. SIMULATION RESULTS AND ANALYSIS. To verify the effectiveness of the proposed method, a numerical simulation was carried out. Using the relative dynamic motion Equation (2), the relative motion of the deputy spacecraft was designed and propagated (Xing et al., 2007; Ou and Zhang, 2017b). Table 1 gives the physical parameters of the chief spacecraft and the deputy spacecraft. Table 2 lists the initial relative state vector of the deputy spacecraft in the LVLH frame. Figure 5 shows the reference relative motion

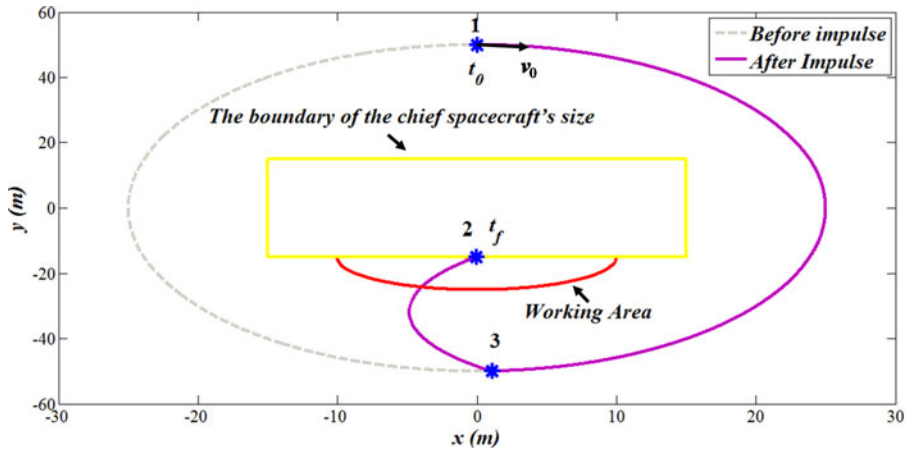


Figure 5. The reference relative motion of the deputy spacecraft.

Table 1. The physical parameters of the deputy spacecraft and chief spacecraft.

The chief spacecraft		The deputy spacecraft	
Parameters	Values	Parameters	Values
Side length/m	30	Mass/kg	50
		Max propulsion/N	30

Table 2. The initial relative state vector of the deputy spacecraft in the LVLH frame.

x (m)	y (m)	v_x (m/s)	v_y (m/s)
0	50	2.766957×10^{-2}	-9.051367×10^{-9}

of the deputy spacecraft. There are three blue asterisks, which are asterisks 1, 2, and 3. The deputy spacecraft begins at asterisk 1 with the initial relative velocity v_0 and flies around the chief spacecraft along the grey trajectory without any transfer impulse. Then, the deputy spacecraft arrives at asterisk 3 and the transfer impulse is implemented on the deputy spacecraft to reach asterisk 2. According to the pulse rendezvous for orbital transformation, we compute the control impulse as Table 3 shows. Table 3 lists the initial impulse control. The purple curves are the reference relative trajectories and the yellow curve is the boundary of the chief spacecraft's size. Moreover, the working area is defined as the area where the deputy spacecraft will execute further operations, such as space inspection and maintenance. A circle is centred on the planned terminal position asterisk 2 and has a certain radius. The working area is the overlap part between the circle and outside the yellow curve.

The final condition is $t_f = 3,400s$ and the radius of the working area is 10 m. Both the frequency of the delta velocity manoeuvres and the integration step are 1 s. The semi-major axis and the eccentricity of the orbit of the chief spacecraft are 6,778.1336 km and 0, respectively, $\lambda_0 = 30$ and $d_0 = 3$. The distribution with respect to the navigation uncertainty is assumed as an uncorrelated zero-mean Gaussian (Psiaki, 2011; Peynot et al., 2014).

Table 3. The initial impulse control in the LVLH frame.

The pulse	u_1	u_2
t (s)	2800	3400
v_{x-t} (m/s)	-9.412288×10^{-3}	2.249601×10^{-2}
v_{y-t} (m/s)	5.155332×10^{-2}	-3.22202×10^{-2}

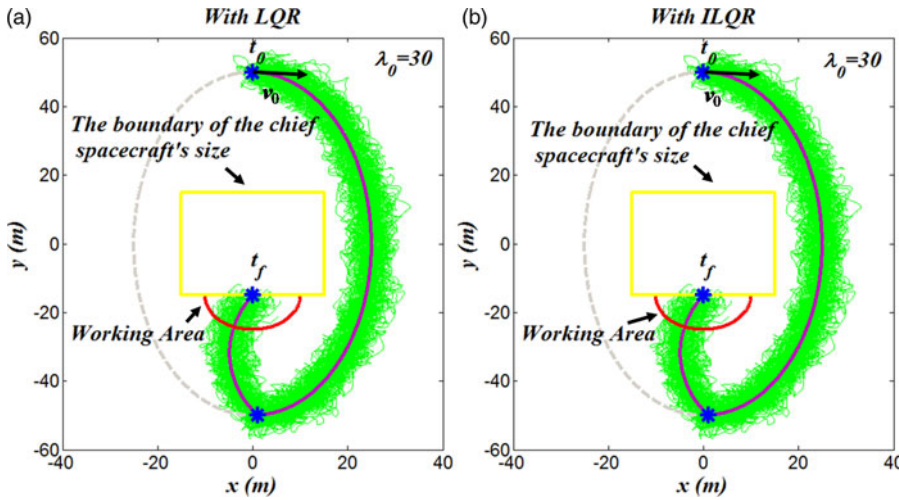


Figure 6. The trajectory of the deputy spacecraft over 100 Monte Carlo runs.

Moreover, the covariance matrix is given as follows (Luo et al., 2011):

$$C_{\delta x_0} = \text{diag}([16, 16, 1.6 \times 10^{-3}, 1.6 \times 10^{-3}]) \tag{87}$$

In this simulation, $Q = \text{diag}[10^{-14}, 10^{-14}, 0, 0]$; $R = \text{diag}[10^{-8}, 10^{-8}]$ and the gravitational constant of Earth is $3.986 \times 10^{14} m^3/s^2$.

6.1. Case with ECPC method with $\lambda_0 = 30$. In this section, we utilise the traditional ECPC method to avoid collision. Figures 6(a) and 6(b) show the actual trajectory of the deputy spacecraft over 100 Monte Carlo runs with a LQR controller and ILQR controller, respectively. The yellow curve is the boundary of the chief spacecraft’s size and the purple curve is the reference relative trajectory of the deputy spacecraft. The red curve is the boundary of the working area. Meanwhile, the green region is the actual trajectory of the deputy spacecraft over 100 Monte Carlo runs. According to Figure 6, when only the ECPC method is executed on the deputy spacecraft, the deputy spacecraft does collide with the chief spacecraft in the presence of a convex polygon shape.

Figure 7 illustrates the values of collision probability over 100 Monte Carlo runs. The blue part is the value of collision probability and the light green part is the ratio of safe missions. From Figure 7, a collision between the deputy spacecraft and the chief spacecraft will occur. Furthermore, the collision probabilities with respect to the LQR controller and the ILQR controller are 31% and 33%. Thus, from Figures 6 and 7, we can conclude that the ECPC method does not solve the safe proximity problem in the presence of a convex polygon shape.

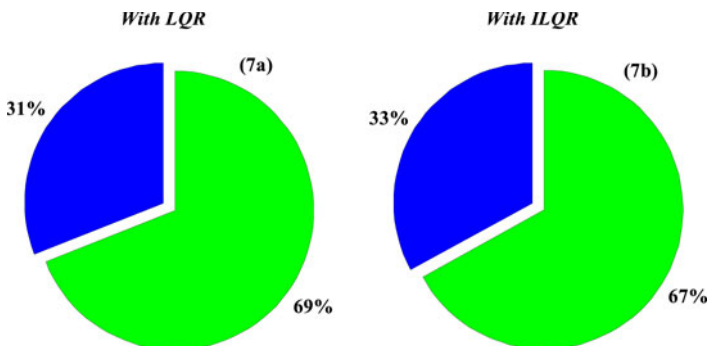


Figure 7. The values of collision probability over 100 Monte Carlo runs.

For comparison, 100 independent Monte Carlo runs were executed under the same conditions, and the Root Mean Square Error (RMSE) in position was calculated as a performance metric. The RMSE is given as (Chen et al., 2018):

$$RMSE = \sqrt{Num^{-1} \sum_{i=1}^{Num} (z_1 - z_2)^2} \tag{88}$$

where *Num* represents the total number of iterations. z_1 and z_2 represent two different series of data. In this paper, the two different series are the actual trajectory and the reference trajectory in the x and y directions.

Figure 8 depicts a comparison of RMSE behaviours in the x and y directions. Based on the ECPC method with the LQR controller, the brown curve and the pink curve represent the RMSE value in the x and y directions, respectively. Combining the ECPC method and the ILQR controller, we can obtain the blue curve and the green curve. The blue curve and the green curve are the RMSE values with respect to the x direction and y directions. From Figure 10, the RMSE values with the LQR controller are larger than those with the ILQR controller. Compared with the LQR controller, the ILQR controller obtains higher control accuracy in the influence of uncertainties. In other words, the robustness of the system is strengthened.

Figure 9 illustrates the associated velocity increment consumptions over 100 Monte Carlo runs. The green curve and the blue curve are the velocity increment consumptions of the deputy spacecraft with the ILQR controller and the LQR controller, respectively. The green curve fluctuates between 90 m/s and 95 m/s while the blue curve is around 89 m/s. From Figure 9, the deputy spacecraft with a ILQR controller requires more fuel. The reason is that $K_4/m^2 + Q$ in the ILQR controller is larger than Q in the LQR controller while the R in the two methods have equal values.

Figure 10 depicts the collision probability and the successful rate of arrival at the working area with different values of λ_0 over 100 Monte Carlo runs. The blue curve is the collision probability and the green curve represents the success rate. From Figure 10, if we adopt the ECPC method with different values of λ_0 , collisions do also take place and the safe proximity problem in the presence of the convex polygon shape is not solved.

6.2. Case with MECPC method with $\lambda_0 = 30$. To solve the safe proximity problem in the presence of a convex polygon shape, the MECPC method is proposed to generate the

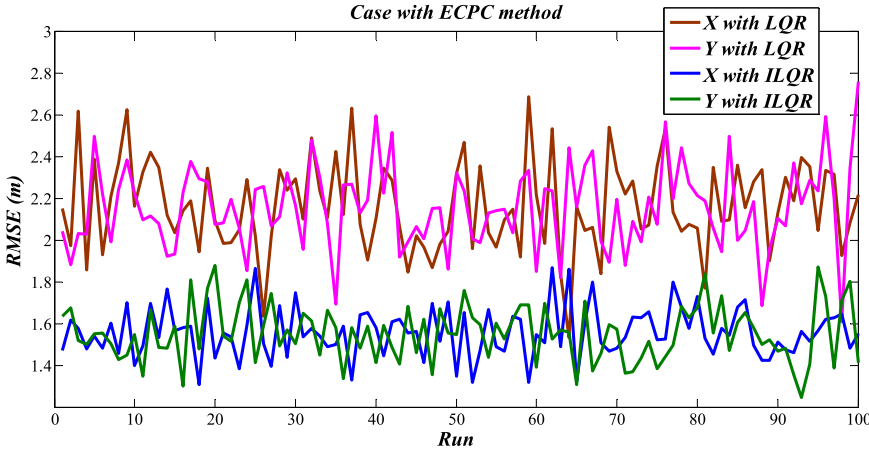


Figure 8. Comparison with respect to the RMSE in two directions.

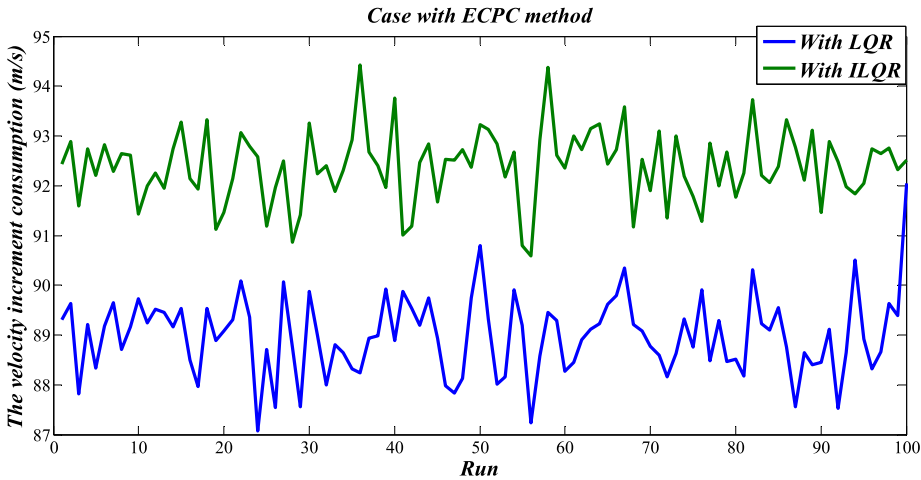


Figure 9. The velocity increment consumptions over 100 Monte Carlo runs.

avoidance manoeuvres. Figure 11 shows the actual trajectory of the deputy spacecraft over 100 Monte Carlo runs. The yellow curve and the purple curve represent the boundary of the chief spacecraft’s size and the reference relative trajectory of the deputy spacecraft. The red curve is the boundary of the working area and the green zone is the actual trajectory of the deputy spacecraft over 100 Monte Carlo runs. From Figure 11, as the avoidance manoeuvres generated by the MECPC method are implemented, the deputy spacecraft successfully avoids collision with the chief spacecraft.

Figure 12 shows the comparison of RMSE behaviours in the x and y directions. According to the MECPC method with the LQR controller, we get the brown curve and the pink curve. The brown curve and the pink curve represent the RMSE values with respect to the x and y directions. The blue curve and the green curve are the RMSE values in the x and y directions, respectively. From Figure 12, the RMSE values with the ILQR controller

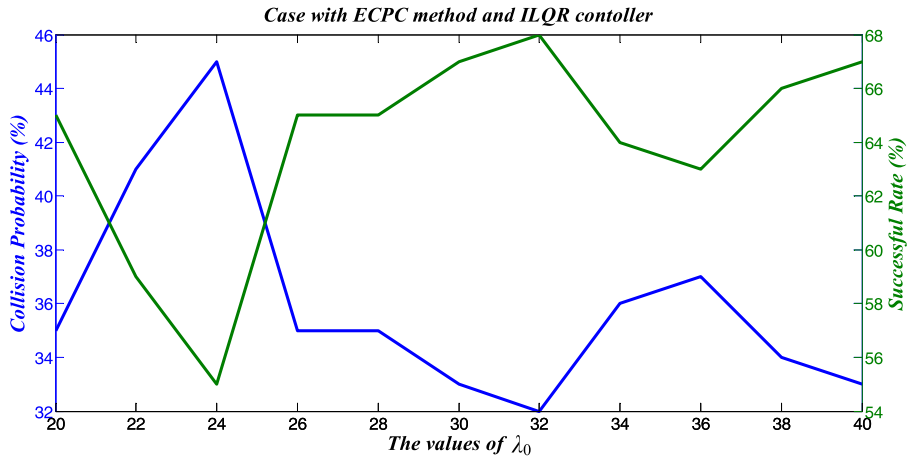


Figure 10. The collision probability and the successful rate with different values of λ_0 over 100 Monte Carlo runs.

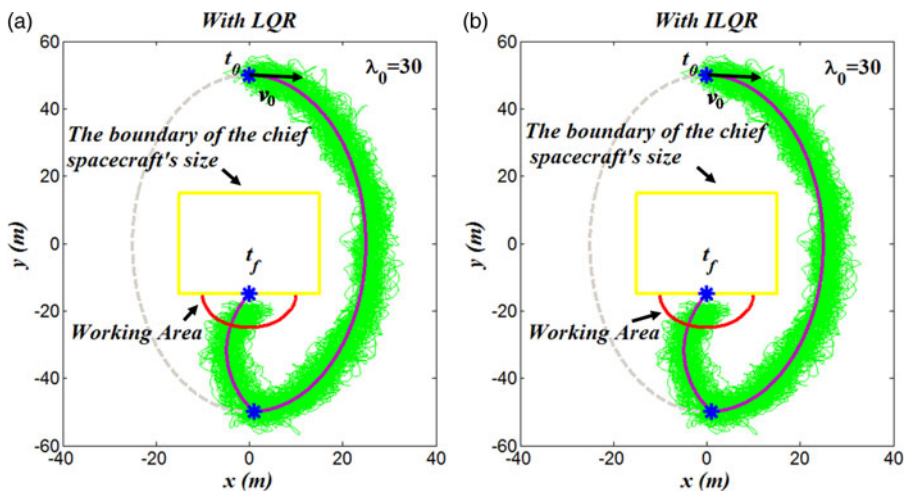


Figure 11. The actual trajectory of deputy spacecraft over 100 Monte Carlo runs.

are lower than the values with the LQR controller. Therefore, the ILQR controller obtains higher control accuracy.

Figure 13 illustrates the associated velocity increment consumptions over 100 Monte Carlo runs. The blue curve and the green curve represent the velocity increment consumptions of the deputy spacecraft with the LQR controller and the ILQR controller, respectively. The green curve is about 94 m/s and the blue curve fluctuates around 90 m/s. Comparing the two curves in Figure 13, the deputy spacecraft with the ILQR controller requires more fuel.

7. CONCLUSIONS. A MECPC method was developed for the spacecraft close-range safe proximity manoeuvre problem for a chief spacecraft with a convex polygon shape.

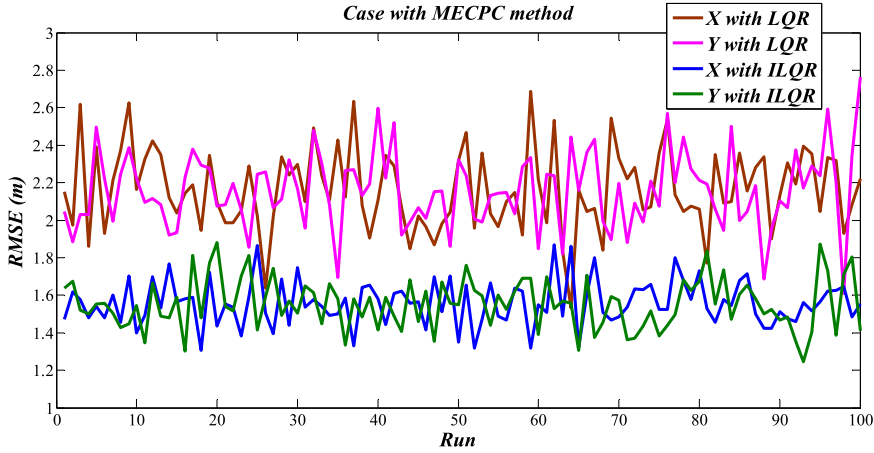


Figure 12. Comparison with respect to RMSE in two directions.

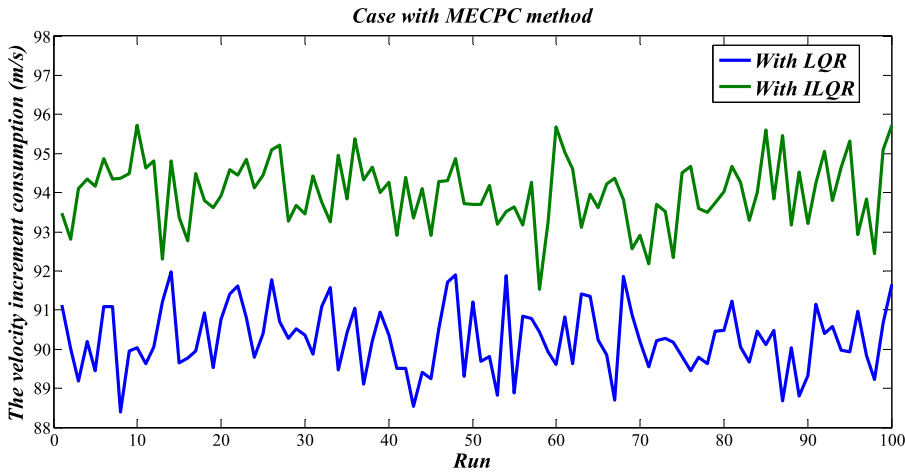


Figure 13. The velocity increment consumptions over 100 Monte Carlo runs.

Compared with the ECPC method, the proposed MECPC method retains advantages such as enhanced robustness against control and navigation uncertainties and has easy theoretical verification of its ability to avoid collision. The MECPC method solves the close-range safe proximity problem considering the influence of the convex polygon shape. Also, an ILQR controller was designed to track the expected trajectory. Finally, numerical simulations are presented to show the effectiveness of the novel MECPC method.

ACKNOWLEDGEMENTS

The work was supported by the Major Program of National Nature Science Foundation of China under Grant Numbers 61690210 and 61690213, the National Science Foundation of China (Grant no. 61503414 and 11404405), and the Scientific Research Project of National University of Defense Technology (Grant no. ZK16-03-20).

REFERENCES

- Alfano, S. (2006a). Satellite Collision Probability Enhancements. *Journal of Guidance, Control, and Dynamics*, **29**(3), 588–592.
- Alfano, S. (2006b). Addressing Nonlinear Relative Motion for Spacecraft Collision Probability. In: *AIAA/AAS Astrodynamics Specialist Conference and Exhibit, Keystone, Colorado*, AIAA paper 2006–6760.
- Bai, X. Z., Chen, L. and Tang, G. J. (2013). Explicit Expression of Collision Probability in terms of RSW and NTW components of relative position. *Advances in Space Research*, **52**(6), 1078–1096.
- Bai, X. Z., Ma, C. W., Chen, L. and Tang, G. J. (2016). Maximum Collision Probability considering Variable Size, Shape, and Orientation of Covariance Ellipse. *Advances in Space Research*, **58**(6), 950–966.
- Bevilacqua, R., Lehmann, T. and Romano, M. (2011). Development and Experimentation of LQR/APF Guidance and Control for Autonomous Proximity Maneuvers of Multiple Spacecraft. *Acta Astronautica*, **68**(7), 1260–1275.
- Cao, L., Chen, X. Q. and Misra, A. K. (2014). Minimum Sliding Mode Error Feedback Control for Fault Tolerant Reconfigurable Satellite Formation with J2 Perturbation. *Acta Astronautica*, **96**, 201–216.
- Cao, L., Qiao, D. and Xu, J. W. (2018a). Suboptimal Artificial Potential Function Sliding Mode Control for Spacecraft Rendezvous with Obstacle Avoidance. *Acta Astronautica*, **143**, 133–146.
- Cao, L., Qiao, D. and Chen, X. Q. (2018b). Laplace ℓ_1 Huber Based Cubature Kalman Filter for Attitude Estimation of Small Satellite. *Acta Astronautica*, **148**, 48–56.
- Chen, Q., Yin, C., Zhou, J., Wang, Y., Wang, X. Y. and Chen, C. Y. (2018). Hybrid Consensus-based Cubature Kalman Filtering for Distributed State Estimation in Sensor Networks. *IEEE Sensors Journal*, **18**(11), 4561–4569.
- Demars, K. J., Cheng, Y. and Jah, M. K. (2014). Collision Probability with Gaussian Mixture Orbit Uncertainty. *Journal of Guidance, Control, and Dynamics*, **37**(3), 979–985.
- Flores-Abad, A., Ma, O., Pham, K. and Ulrich, S. (2014). A Review of Space Robotics Technologies for On-orbit Servicing. *Progress in Aerospace Science*, **68**, 1–26.
- Ge, S. S., Cui, Y. J. (2002). Dynamic Motion Planning for Mobile Robots using Potential Field Method. *Autonomous Robots*, **13**(3), 207–222.
- Huang, X., Yan, Y., Zhou, Y. and Yang, Y. N. (2017a). Dual-quaternion based Distributed Coordination Control of Six-DOF Spacecraft Formation with Collision Avoidance. *Aerospace Science and Technology*, **67**, 443–455.
- Huang, X., Yan, Y. and Zhou, Y. (2017b). Underactuated Spacecraft Formation Reconfiguration with Collision Avoidance. *Acta Astronautica*, **131**, 166–181.
- Lin, F. (2007). *Robust Control Design an Optimal Control Approach*. John Wiley & Sons Ltd, The Atrium, Southern Gate, Chichester, England, Ch. 5.
- Luo, Y. Z., Liang, L. B., Wang, H. and Tang, G. J. (2011). Quantitative Performance for Spacecraft Rendezvous Trajectory Safety. *Journal of Guidance, Control, and Dynamics*, **34**(4), 1264–1269.
- Luo, Y. Z. and Yang, Z. (2017). A Review of Uncertainty Propagation in Orbital Mechanics. *Progress in Aerospace Sciences*, **89**, 23–39.
- Nag, S. and Summerer, L. (2013). Behaviour based, Autonomous and Distributed Scatter Manoeuvres for Satellite Swarms. *Acta Astronautica*, **82**(1), 95–109.
- Ni, Q., Huang, Y. Y. and Chen, X. Q. (2016). Nonlinear Control of Spacecraft Formation Flying with Disturbance Rejection and Collision Avoidance. *Chinese Physics B*, **26**(7), 014502.
- Ou, Y. W. and Zhang, H. B. (2017a). Observability-based Mars Autonomous Navigation Using Formation Flying Spacecraft. *Journal of Navigation*, **71**(1), 21–43.
- Ou, Y. W. and Zhang, H. B. (2017b). Mars Final Approach Navigation using Ground Beacons and Orbiters: An Information Propagation Perspective. *Acta Astronautica*, **138**, 490–500.
- Palacios, L., Ceriotti, M. and Radice, G. (2015). Close Proximity Formation Flying via Linear Quadratic Tracking Controller and Artificial Potential Function. *Advances in Space Research*, **56**(10), 2167–2176.
- Patera, R. P. (2003). Satellite Collision Probability for Nonlinear Relative Motion. *Journal of Guidance, Control, and Dynamics*, **26**(5), 728–733.
- Patera, R. P., (2006). Collision Probability for Larger Bodies Having Nonlinear Relative Motion. *Journal of Guidance, Control, and Dynamics*, **29**(6), 1468–1472.
- Peynot, T., Lui, S. T., McAllister, R., Fitch, R. and Sukkarieh, S. (2014). Learned stochastic mobility prediction for planning with control uncertainty on unstructured terrain. *Journal of Field Robotics*, **31**(6), 969–995.
- Psiaki, M. L. (2011). Absolute orbit and gravity determination using relative position measurements between two satellites. *Journal of Guidance, Control, and Dynamics*, **34**(5), 1285–1297.

- Serra, R., Arzelier, D., Joldes, M., Lasserre, J. B., Rondepierre, A. and Salvy B. (2016). Fast and Accurate Computation of Orbital Collision Probability for Short-Term Encounters. *Journal of Guidance, Control, and Dynamics*, **39**(5), 1009–1021.
- Shan, M. H., Guo, J. and Gill, E. (2016). Review and Comparison of Active Space Debris Capturing and Removal Methods. *Progress in Aerospace Science*, **80**, 18–32.
- Spencer, D. A., Chait, S. B., Schulte, P. Z. and Okseniuk, K. J. (2016). Prox-1 University-Class Mission to Demonstrate Automated Proximity Operations. *Journal of Spacecraft and Rockets*, **53**(5), 847–863.
- Sun, Z. J., Luo Y. Z. and Niu, Z. Y. (2014). Spacecraft Rendezvous Trajectory Safety Quantitative Performance Index Eliminating Probability Dilution. *Science Chin Technological Sciences*, **57**(6), 1219–1228.
- Vittaldev, V., Russell, R. P. and Linares, R. (2016). Spacecraft Uncertainty Propagation Using Gaussian Mixture Models and Polynomial Chaos Expansions. *Journal of Guidance, Control, and Dynamics*, **39**(12), 2615–2626.
- Wang, Y., Bai, Y. Z., Ran, D. C., Zhao, Y., Zhang, X. and Chen, X. Q. (2017). The Equal-collision-probability-surface for Spacecraft Collision Avoidance. In: *3rd IAA Conference on Dynamics and Control of Space Systems, Moscow*, IAA-AAS-DyCoss3-037.
- Wang, Y., Bai, Y. Z., Xing, J. J., Gianmarco, R., Ni, Q., Chen, X. Q. (2018). Equal-collision-probability-curve method for Safe Spacecraft Close-range Proximity Maneuvers. *Advance in Space Research*, 2018. doi:10.1016/j.asr.2018.07.007.
- Xing, J. J., Tang, G. J., Xi, X. N. and Li, H. Y. (2007). Satellite Formation Design and Optimal Stationkeeping Considering Nonlinearity and Eccentricity. *Journal of Guidance, Control, and Dynamics*, **30**(5), 1523–1528.
- Xing, J. J., Yu, Y., Wang, Y., Zheng, L. M. and Chen, Z. A. (2016). Robust Control of Low Earth Satellites Formation Based on Improved Linear Quadratic Regular. *Journal of National University of Defense Technology*, **38**(3), 100–106. (in Chinese)
- Yang, Z., Luo, Y. Z., Zhang, J. and Tang, G. J. (2016). Uncertainty Quantification Short Rendezvous Missions Using a Nonlinear Covariance Propagation Method. *Journal of Guidance, Control, and Dynamics*, **39**(9), 2167–2175.
- Yu, J., Chen, X. Q., and Chen, L. H. (2015). Optimal Planning of LEO Active Debris Removal based on Hybrid Optimal Control Theory. *Advances in Space Research*, **55**(11), 2628–2640.